Article

Not peer-reviewed version

Enhanced Metal-Support Inteaction in Ni/Biomass-Derived Carbon Catalyst via AtomicNi-N_4 Sites for Boosting Dye-Sensitized Photocatalytic H_2 Production

Weiying Zhang *, Tian Liao , Niuniu Guo , Shiyu Liu , Shaoqin Peng , Yuexiang Li *

Posted Date: 16 December 2025

doi: 10.20944/preprints202512.1450.v1

Keywords: biomass-derived carbon; metal-support interaction; atomic Ni-N4 sites; dye-sensitized photocatalytic; hydrogen evolution reaction

 doi:10.20944/preprints202512.1450.v1

Article

Enhanced Metal-Support Inteaction in Ni/Biomass-Derived Carbon Catalyst via Atomic Ni-N_4 Sites for Boosting Dye-Sensitized Photocatalytic H_2 Production

Weiying Zhang *, Tian Liao, Niuniu Guo, Shiyu Liu, Shaoqin Peng and Yuexiang Li *

School of Chemistry and Chemical Engineering, Key Laboratory of Jiangxi Province for Environment and Energy Catalysis, Nanchang University, Nanchang, 330010, China

* Correspondence: zhangwy@ncu.edu.cn (W.Y.Z.); liyx@ncu.edu.cn (Y.X.L.)

Abstract

It is of great significance to prepare carbon supported non-noble metal catalysts for hydrogen evolution reaction (HER) via a sustainable method. Meanwhile, the enhanced metal-support interaction (MSI) is vital for promoting the catalytic activity of metal/carbon catalysts. Herein, we prepare biomass-derived porous carbon supported metal Ni catalyst (Ni/APC) with the enhanced MSI via atomic Ni-N_4 sites utilizing agaric as a precursor. The highly dispersed Ni-N_4 species preferentially adsorb dye molecules and reactant H_2O, beneficial to efficient electron transfer and promoting H_2O dissociation. Meanwhile, Ni nanoparticles undertake the active sites for H_2 desorption. In virtue of the synergistic effect of metal Ni nanoparticles and atomic Ni-N_4 for different roles of active sites, Ni/APC catalysts show more effective dye-sensitized photocatalytic HER activities, compared with pure Ni and pure APC. The Ni/APC catalyst with an optimal Ni loading amount exhibits a high AQY of 41.0 % with an excellent long-term stability in terms of both HER activity and structure. It is the first report of an application for biomass-derived carbon catalysts in dye-sensitization hydrogen production, and the synergistic effect of atomic Ni and particled Ni on the dye-sensitized photocatalytic HER is deeply investigated. This work provides new deep insight into the design of new non-noble metal/carbon materials by taking advantages of biomass materials.

Keywords: biomass-derived carbon; metal-support interaction; atomic Ni-N_4 sites; dye-sensitized photocatalytic; hydrogen evolution reaction

1. Introduction

Producing clean H_2 from renewable solar energy fuel production via photocatalysis is a promising low-carbon strategy to address the current energy crisis and environmental issues [1–3]. In dye-sensitized photocatalytic hydrogen evolution reaction (HER) system, the cocatalyst is an important constituent to improve the separation of photogenerated electrons and holes and serves as the active sites for hydrogen production [4,5]. Noble metal Pt is considered as the most efficient cocatalyst, however, its low abundance and high price greatly prevent its large-scale application in industry [6–8]. As the desirable alternatives, a lot of transition metals [9–11] and compounds [12–14] have been studied for photocatalytic HER. In usual cases, metal-based cocatalysts are supported on carbon materials including carbon nanotubes [15], graphene [16] and carbon nanosheets [17] to inhibit their aggregation, which is very necessary to ensure sufficient active sites for longlasting catalysis. Considering the high preparation cost of the above carbon materials, the carbonization of inexpensive biomass with inherent structure diversity is a simple and cost-effective way to produce desired carbon-based catalysts.

 doi:10.20944/preprints202512.1450.v1

Agaric (or wood ear), a worldwide abundant fungus with a fast growth rate, can be used as a promising precursor to prepare carbon-based catalysts with transition metal components [18–20]. Specifically, the super high water-absorption capacity makes dired agaric a great precursor to preprare carbon-based catalysts loaded with transition metal or compounds [21,22]. Up to now, however, the application for agaric-derived carbon catalysts in dye-sensitized hydrogen production has not been reported.

In the dye-sensitized HER system, the interaction between the dye and the cocatalyst plays a significant role in promoting the HER activity. Commonly, as for the carbon-based cocatalysts, the injection of photo-induced electrons from dyes always depends on the π-π stacking interaction between dye molecules and carbon materials, such as graphene or carbon nanotubes [4,23]. However, this interaction is weak and leads to ineffective injection of photo-induced electrons. Therefore, constructing carbon materials that can exert stronger interaction with dye molecules, such as electrostatic interaction, should be effective to facilitate the electron injection. To this end, N element in agaric can provide the coordination sites for single atomic metal, like Co, Ni, Fe. [24–26] Owing to the larger electronegativity of N element, these atomic metals often possess positive charges, which can form electrostatic interactions with negatively charged dyes, such as Eosin Y (EY), one of xanthene dyes. This electrostatic force will enable the cocatalysts with a greater adsorption capacity of dyes, and more dye-excited electrons can be injected onto the cocatalyst.

Herein, Herein, as illustrated in Figure 1a, atomic Ni and nanoparticled Ni on agaric-derived porous carbon (APC) were fabricated, and firstly reported for the application of biomass-derived carbon material in dye-sensitized photocatalytic HER. Metal Ni nanoparticles with the diameter of dozens of nanometers are supported on the stacked porous carbon sheets. Besides, the presence of N elements in agaric results in the formation of Ni-N_4 sites in APC sheets. This highly dispersed Ni-N_4 species are conducive to the adsorption of dye molecules, allowing their electrons to be rapidly injected onto the surface of the cocatalyst. At the same time, this positively charged Ni-N_4 sites can facilitate the dissociation of water molecules into OH^- and H^+, and the latter quickly accept the injected electrons to form hydrogen atoms. Metal Ni nanoparticles serve as the active sites for hydrogen adsorption and desorption. These features endow Ni/APC composites with much enhanced HER activities, compared to APC, Ni, and atomic Ni/APC, presenting synergistic effect of Ni-N_4 species and Ni nanoparticles..

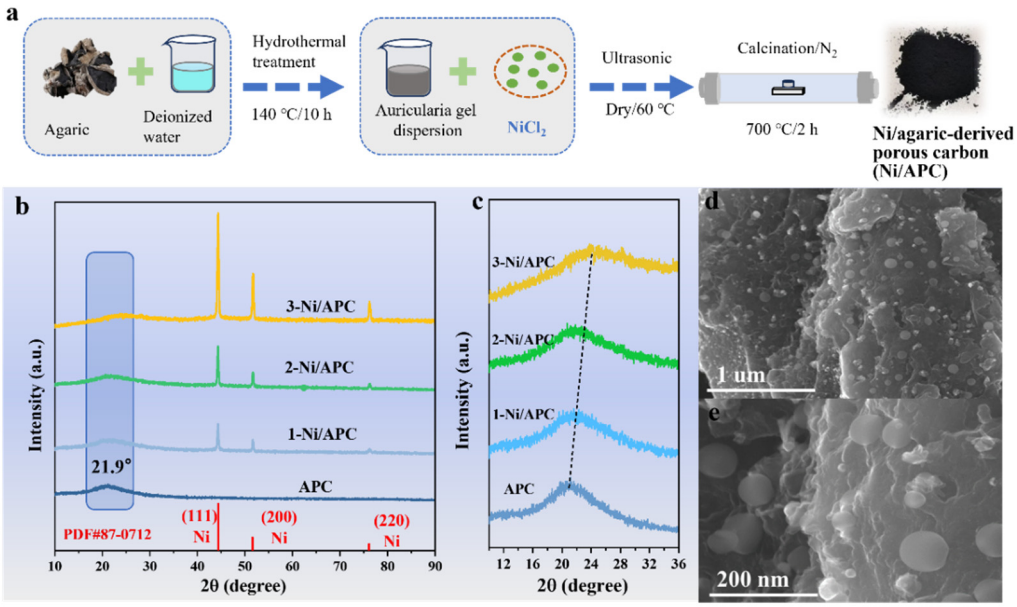

Figure 1. (a) Schematic illustration of the preparation of Ni/APC composites. (b, c) XRD patterns of APC and x-Ni/APC composites, and (d, e) SEM images of 2-Ni/APC composite.

 doi:10.20944/preprints202512.1450.v1

2. Materials and Methods

2.1. Materials

Agaric was purchased from the market, and nickel chloride hexahydrate ($NiCl_2{\cdot}6H_2O$, AR), EY (BR), trimethylamine (TMA, CP) were purchased from Sinopharm Group Chemical Reagent Co., Ltd.

2.2. Preparation of Ni/Agaric-Derived N-Doped Porous Carbon (APC) Composites

The Ni/agaric-derived N-doped porous carbon composites were prepared by a hydrothermal-impregnation-carbonization approach. In detail, dried agaric was washed by soaking in deionized water for 1 h to remove impurities and dried at 80 °C. Then, the re-dried agaric (4.0 g) and deionized water (60 mL) were transferred into a 100 mL Teflon-lined autoclave, and remained at 140 ° C for 10 h to obtain the agaric hydrogel. The agaric gel (30 mL) was severally added with 0.5, 1, 2, and 3 mmol $NiCl_2 \cdot 6H_2O$ to form a homogeneous dispersion under ultrasonic treatment. The above dispersion was then dried in an oven at 80 ° C, and annealed at 700 °C for 2 h in N_2 atmosphere with a heating rate of 10 °C min^{-1} to prepare Ni/agaric-derived N-doped porous carbon (APC), which were labeled as x-Ni/APC (x = 0.5, 1, 2, 3, x represents the amount of $NiCl_2 \cdot 6H_2O$, mmol). As control, APC sample was prepared by the above method without addition of $NiCl_2 \cdot 6H_2O$, and $NiNO_3 \cdot 6H_2O$ was reduced to pure metal Ni at 700 °C for 2 h in N_2+H_2 atmosphere.

2.3. Characterization

X-ray diffraction (XRD) patterns were recorded with Ni-filtered Cu Kα radiation using an XD-2/3 diffractometer. X-ray photoelectron spectroscopy (XPS) analysis was performed on a spectrometer equipped with an Al Kα X-ray source (Thermo Scientific K-Alpha USA). The C1s peak of 284.8 eV was used as an internal reference for the absolute binding energy. Scanning electron microscopy (SEM, FEI Quanta 200, Japan) and transmission electron microscopy images (TEM, Talos F200X, USA) were taken to investigate the microstructure and morphology of the prepared catalysts. XAFS spectra were recorded at room temperature using a 4-channel Silicon Drift Detector (SDD) Bruker 5040. Extended X-ray absorption fine structure (EXAFS) spectra were recorded in transmission/fluorescence mode. Negligible changes in the line-shape and peak position of Ni K-edge XANES spectra were observed between two scans taken for a specific sample. The spectra were processed and analyzed by the software codes Athena.

Fluorescence test was performed on Hitachi FL-7000. The dispersion was prepared as follows: 20 mg x-Ni/APC catalyst was added into 100 mL of eosin Y solution (EY, 1×10^{-5} mol L^{-1}), and then sonicated for 2 h. The excited wavelength was 470 nm.

2.4. Photocatalytic Performance

The photocatalytic HER was carried out under visible light irradiation in a 190 mL closed light flask with an effective irradiation area of about 19.6 cm^2. A 400 W high-pressure mercury lamp was used as the light source (incident light intensity 25 m W cm-2) with a truncated glass filter ($\lambda \leq 420$ nm) and a water-cooled jacket to eliminate ultraviolet and infrared light, ensuring only visible light irradiation. Typically, 100 mg x-Ni/APC cocatalyst, 5 mL EY (1.0×10^{-2} mol L^{-1}) and 95 mL TMA solution (pH=11.0) were added together, and the dispersion was sonicated for 5 min and degassed for 25 min with N_2. The amount of H_2 product was determined by gas chromatograph.

The stability test was carried out under the same conditions of the above photocatalytic hydrogen reaction by replacing the fresh dye and sacrifice agent after each cycle. Apparent quantum yield (AQY) was calculated according to formula (1). LEDs with different wavelengths (UVEC-4) were used as light source.

$$AQY\ [\%] = 2\times(\text{mole of } H_2)/(\text{mole of incident photon}) \times 100 \quad (1)$$

 doi:10.20944/preprints202512.1450.v1

2.5. Electrochemical Test

Linear scanning voltammetry (LSV) curves of APC and x-Ni/APC catalysts in 1.0 M KOH solution were obtained using an electrochemical workstation (CHI600E). To prepare the working electrodes, 5.0 mg catalyst and 10 μL Nafion solution were dispersed in 1.0 mL deionized water, and then sonicated for 4 h to form a homogeneous dark dispersion. Then, 10 μL of the dispersion was dropped onto a clean glassy carbon electrode with a diameter of 3 mm for nature drying, repeating the preceding steps four times. Pt wire and Hg/HgO electrode were used as the counter and reference electrodes, respectively. The scan range was -0.924 to -1.524 V with a scan rate of 10 mV s^{-1}. The voltage to a reversible hydrogen electrode (RHE) can be converted according to the following equation:

$$E_{(RHE)} = E_{(Hg/HgO)} + 0.098\ V + 0.0591\ pH \quad (2)$$

The electrochemically active surface area (ECSA) was evaluated based on double layer capacitance (C_{dl}), which was performed via CV measurements (applied potential of 0.914~1.014 V vs. RHE) at various scan rates (20, 40, 60, 80, and 100 mV s^{-1}). The Cdl values were obtained by plotting the current against the scan rates.

Electrochemical impedance spectroscopy (EIS) tests were performed on a three-electrode cell on an electrochemical workstation of IVIUMSTAT (the Netherlands). The test conditions were as follows: Pt wire was used as the counter electrode and Ag/AgCl as the reference electrode. The working electrode was prepared as same to the LSV test except the dispersion amount (20 μL). The electrolyte solution was 0.1 M phosphate buffer solution (PBS, pH=7.0).

The dye-sensitization photocurrent tests of Ni/APC cocatalysts were performed on a CHI660 electrochemical workstation. The dispersion was prepared similar to LSV test. 100 μL of the as-prepared dispersion was dropped onto FTO conductive glass with a valid area of 1×1 cm^2. Pt wire electrode and Ag/AgCl electrode were applied as the counter and the reference electrode, respectively. The electrolytes were 0.1 mol L^{-1} Na_2SO_4 solution including trimethylamine (pH = 11.0) and EY solution (5.0×10^{-4} mol L^{-1}). 400 W Xe lamp was used as the irradiation source.

3. Results

Phase purity of the as-prepared composites was analyzed by X-ray diffraction (XRD). As shown in Figure 1b, for all the composites, the broad peak around 21.9° is assigned to graphite carbon (002) diffraction, indicating the successful carbonization of biomass agaric [27]. In the case of Ni/APC composites, there are three representative peaks appearing at 44.5°, 51.8° and 76.4°, which correspond to (111), (200) and (220) planar diffraction of the face-center cubic structure of metal Ni (PDF #87-0712) respectively. The calculated crystal sizes of metal Ni based on Scherrer formula for 1-Ni/APC, 2-Ni/APC, 3-Ni/APC were 29.5, 32.3, 33.6 nm, respectively. It is worth noting that the peak of graphite carbon shifts positively (Figure 1c). Thus, the introduction of metal Ni promotes the carbonization degree of APC [28], which is beneficial to the electron transfer. Figure 1d,e show the SEM images of 2-Ni/APC composite. The lamellar structure of APC can be clearly observed, and a great number of metal Ni nanoparticles with the diameter of dozens of nanometers are distributed uniformly on the carbon layers. Figure S1 presents the high-resolution SEM images of 1-Ni/APC, and 3-Ni/APC composites. It is found that the size of Ni nanoparticles of x-Ni/APC composites increases with the Ni loading amounts, consistent with the results obtained by XRD.

The microstructures of APC and 2-Ni/APC are further investigated by TEM and HRTEM. Figure 2a,b show the TEM images of APC, and it can be observed that the APC surface was smooth, and heavily stock together each other with the large block state. While 2-Ni/APC composite (Figure 2c) clearly presents dark Ni nanoparticles distributed on carbon layers, and the carbon substrate of 2-Ni/APC shows rough surface and thinner thickness. Besides, there are many pores existing around Ni particles. The enlargements of Figure 2c clearly show the pores with the size of a few tens of nanometers. These pores contribute to 2-Ni/APC composite with a fluffy appearance. Figure S2 provides the N_2 adsorption-desorption isotherms of APC and 2-Ni/APC. 2-Ni/APC catalyst exhibits

 doi:10.20944/preprints202512.1450.v1

much higher specific surface area (74.1 $m^2 g^{-1}$) and porosity, compared with APC (5.6 $m^2 g^{-1}$). We speculate that the added $NiCl_2$ which could be as a self-template for the pores. The adsorbed Ni^{2+} in the agaric structure would be recrystallized into $NiCl_2$ particles after drying process. During the later carbonization process, $NiCl_2$ particles are reduced into metal Ni with a volume contraction [29]. As a result, the pores around Ni nanoparticles are produced. These pores and the increased surface area are beneficial to the mass transfer diffusion [4,30]. Figure 2d and the inset show the highly ordered lattice fringes with the lattice spacing of 0.204 nm, which perfectly matches the (111) plane of metal Ni. Figure 2e shows C, and N elements are evenly distributed on carbon layers of 2-Ni/APC catalyst, indicating N doped carbon material is formed by the pyrolysis-carbonization of agaric. And the aggregation of Ni element is observed, which fully proves the successful formation of metal Ni. Surprisedly, other unaggregated Ni element also highly disperses on APC substrate, we speculate the presence of single atomic Ni, usually in the form of Ni-N_4 sites in N-doping carbon materials [31–33].

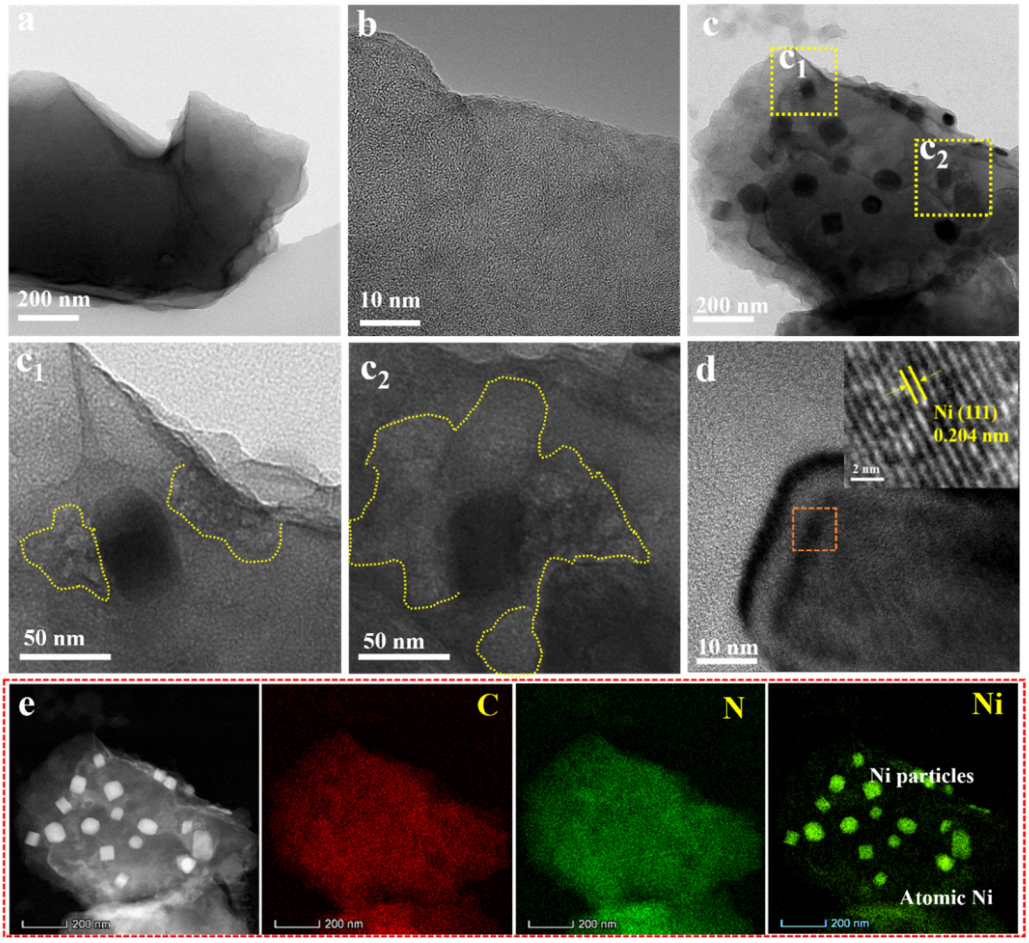

Figure 2. TEM and high-resolution TEM images of (a, b) APC, and (c, d) 2-Ni/APC. (e) Element mapping images of 2-Ni/APC.

In order to affirm single atomic Ni, we treated 2-Ni/APC with HCl to remove Ni nanoparticles (labeled as T-2-Ni/APC). As shown in Figure S3, the result of XRD pattern shows no diffraction peaks of metallic Ni, confirming the removal of Ni nanoparticles. Besides, the T-2-Ni/APC was observed by X-ray absorption spectroscopy (XAS) measurement. Figure 3a depicts the X-ray absorption near-edge structure spectra (XANES) at the Ni K-edge of T-2-Ni/APC with Ni foil, NiO, and nickel phthalocyanine (NiPc) as references. It was observed that the absorption edge of T-2-Ni/APC was slightly higher than that of Ni foil and NiO, however, close to that of NiPc, suggesting that the average chemical state and coordination environment around the Ni species of T-2-Ni/APC was similar to NiPc, where Ni atom forms a coordination bond with the nitrogen atom by Ni-N4 species

 doi:10.20944/preprints202512.1450.v1

[34]. The Fourier-transform (FT) Ni K-edge of the EXAFS for the above samples is presented in Figure 3b. The peak at 1.47 Å of T-2-Ni/APC correspond to Ni-N, in contrast of standard NiPc. The wavelet transform (WT) of the k3-weighted Ni K edge EXAFS spectrum counter plots are further investigated. Compared to Ni foil, NiO, and NiPc references (Figure 3c-e), T-2-Ni/APC (Figure 3f) is almost same to that of NiPc, further evidencing single atom Ni coordination with N atoms. Figure 3g shows the TEM images for T-2-Ni/APC. No Ni particles were observed to be distributed on the agaric-derived carbon sheets. However, Ni element was highly dispersed on APC sheets (Figure 3i-k), which has been fully confirmed that atomic Ni exists in the form of Ni-N. Combining the results of TEM (Figure 2), these results disclosed that Ni nanoparticles and atomic Ni-N species are in-situ formed on APC sheets during the pyrolysis process.

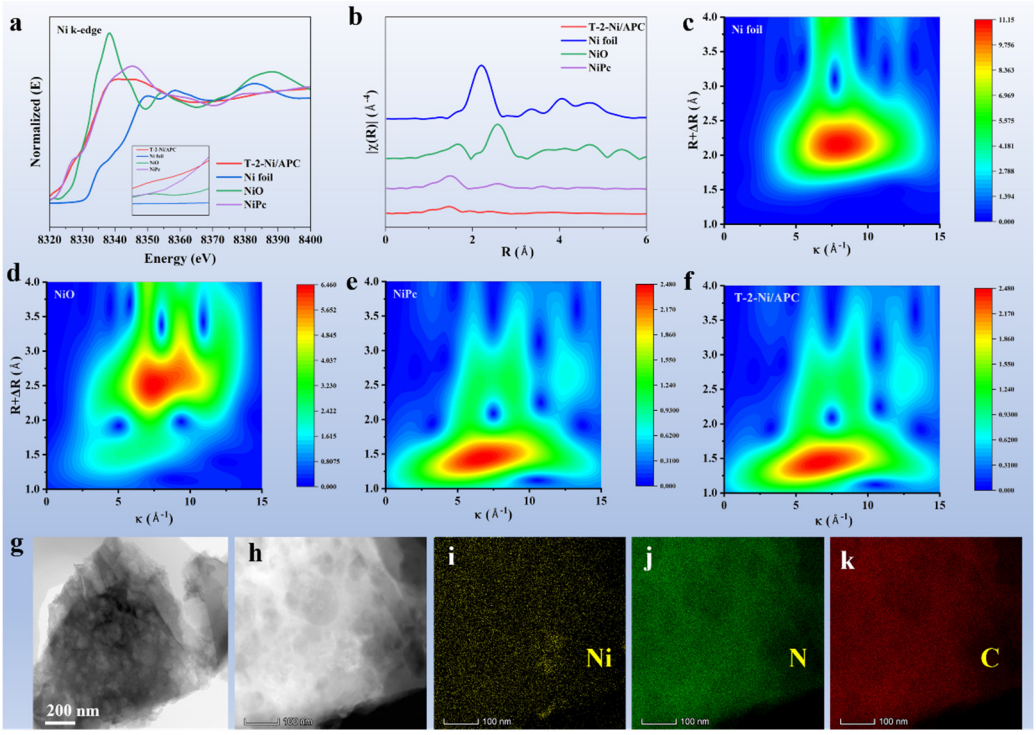

Figure 3. (a) Normalized Ni K-edge XANES spectra, (b) Fourier-transform of Ni K-edge EXAFS, and Wavelet transform spectra of the EXAFS for (c) Ni foil, (d) NiO, (e) NiPc, and (f) T-2-Ni/APC. (g) TEM image and (h-k) elemental mapping images of T-2-Ni/APC.

The chemical states of C, N, and Ni elements on the surface of APC and 2-Ni/APC catalysts were determined by XPS. Elements including C, O, N, and Ni can be detected in 2-Ni/APC by the full XPS spectrum in Figure 4a. Figure 4b shows the high-resolution C 1s XPS spectra of APC and 2-Ni/APC, which can be deconvoluted into four peaks, C=C (284.6 eV), C-C (285.3 eV), C-O/C-N (286.5 eV), and COOH (288.8 eV). The content of -COOH group in 2-Ni/APC composite is significantly reduced compared with APC. While the percentage of the C=C bond peak in 2-Ni/APC is increased to 75.59 %, superior to that of APC (72.09 %). And C/O atom ratio in 2-Ni/APC is 7.85, much higher than that in APC (5.88). All the above parameters suggest that Ni incorporation facilitates the formation of C=C bonds, consistent with XRD results. N 1s spectra in Figure 4c are splitted into four components, namely oxidized nitrogen (403.3 eV), graphitic nitrogen (400.7 eV), pyrrolic N (399.2 eV), and pyridinic N (398.1 eV). Compared with APC, the peaks of pyridinic N and graphitic N in 2-Ni/APC both shift to the higher energy side. In particular, pyridinic N more easily bonds with Ni to form Ni-N4 species [35,36], namely atomic metal sites, as illustrated in Figure S4. Figure 4d exhibits the high-resolution Ni 2p spectra of metal Ni and 2-Ni/APC composite. Ni0 peak in 2-Ni/APC shifts toward lower binding energy (853.1 eV), and the domain peak shifts to the higher binding energy (856.3 eV), confirming the formation of strong metal-support interaction (MSI) via the Ni-N bond between Ni and APC. This MIS could efficiently facilitate the interfacial electron transfer [37].

 doi:10.20944/preprints202512.1450.v1

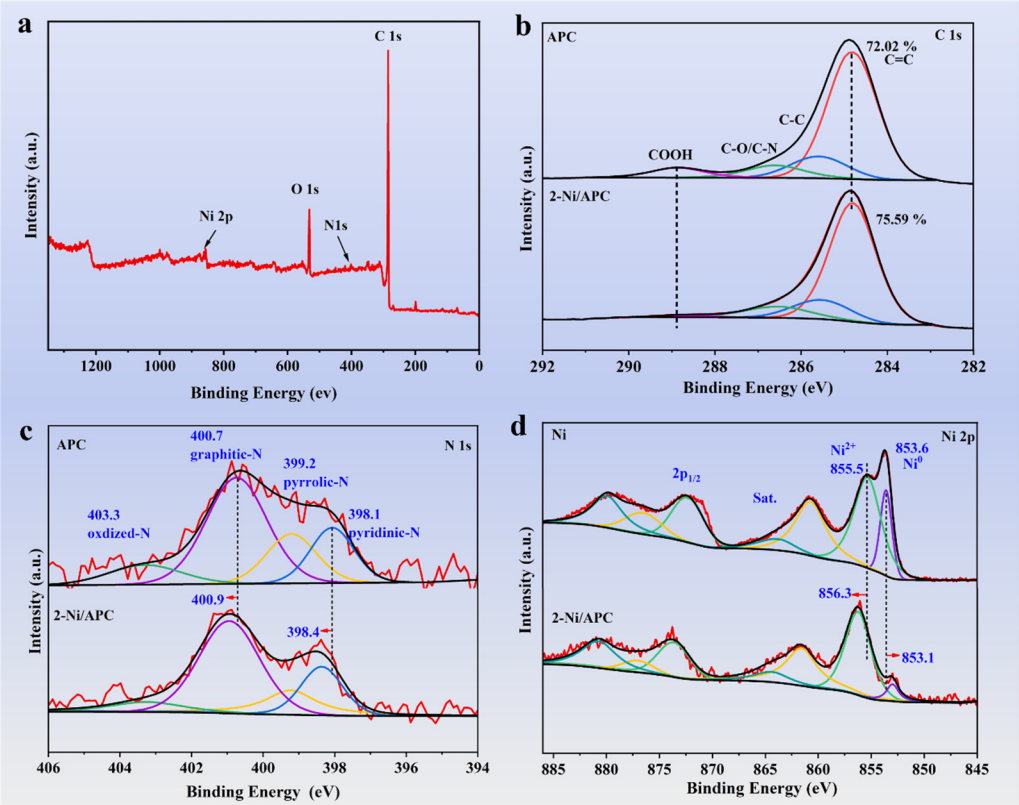

Figure 4. (a) XPS survey of 2-Ni/APC, (b) C 1s and (c) N 1s for APC and 2-Ni/APC, (d) Ni 2p spectra for Ni and 2-Ni/APC.

The above composites containing atomic Ni and particled Ni are adopted as the cocatalysts in the dye-sensitized photocatalytic HER. Figure 5a shows the comparison of the dye-sensitized photocatalytic HER activities for APC, Ni, and Ni/APC cocatalysts. APC shows a low dye-sensitized HER activity (1.2 μmol), which may be related to the defect structure as the active sites for H_2 evolution. Not surprisingly, pure metal Ni exhibits lower activity, just 0.4 μmol because metal Ni without supports is easy to agglomerate and lack active sites. While the Ni/APC cocatalysts present much higher photocatalytic H_2 evolution activities than metal Ni and APC. As the Ni loading amount increases, the activities accordingly increase, and the maximum activity is high up to 114.1 μmol for 2-Ni/APC, displaying the significant synergistic effect. The activity decreases lightly to 105.5 μmol for 3-Ni/APC. We also investigated the dye-sensitized activity of T-2-Ni/APC to evaluate the roles of atomic Ni and particled Ni. As provided by Figure 5b, T-2-Ni/APC exhibits the superior activity to APC, and much inferior to 2-Ni/APC, confirming atomic and particled Ni jointly accelerate HER process. EY molecules as the antenna absorbs light, and its concentration greatly affect the photocatalytic activity. Figure 5c illustrates the effect of EY concentration on the photocatalytic HER activity for 2-Ni/APC composite. When the absence of dye molecules, the system almost did not produce hydrogen due to the lack of the electrons which should be originated from excited dye molecules in light conditions. With the increase of EY concentration from 1×10^{-4} to 6×10^{-4} mol L^{-1}, the hydrogen production amount gradually increases. The activity reaches the maximum value of 117.2 μmol when EY concentration is 6×10^{-4} mol L^{-1}. However, when EY concentration is further increased, the hydrogen evolution activity decreases. The reason is that the high EY concentration can easily cause the self-quenching of fluorescence and form the dimer or trimer of the dye molecules [38]. The apparent quantum efficiency (AQY) is a standard to compare the photocatalytic hydrogen production activity. Figure 5d shows the AQY values of EY-2-Ni/APC system under the different wavelength irradiation. Varying the incident irradiation wavelength from 420 to 600 nm, AQY increases firstly and then decreases. It reaches a maximum of 41.0 % at 450 nm, outperforming many carbon-based materials, as listed Table S1. It is worth mentioning that it is the first report of carbon-supported

 doi:10.20944/preprints202512.1450.v1

cocatalysts derived from biomaterials for dye-sensitization photocatalytic HER application. We further investigate the stability of 2-Ni/APC cocatalyst in dye-sensitized photocatalytic HER. As shown in Figure 5e, the activities remained almost unchanged after seven cycles under the conditions of changing fresh EY/TMA solution in each cycle, proving the excellent stability of the 2-Ni/APC cocatalyst. After the stability test, 2-Ni/APC cocatalyst maintains its diffraction peaks in XRD patterns, as provided in Figure 5f, demonstrating good stability in phase structure. As further revealed by XPS in Figure 5g, Ni 2p spectra of the cycled 2-Ni/APC barely change, in contrast with the fresh one. Combined with C 1s and N 1s XPS spectra (Figure S5), it is believed that the Ni/APC composites are fairly stable after long-term photocatalytic HER. TEM image and elemental maps of cycled 2-Ni/APC are also provided in Figure 5h,i. It can be seen that the pores of APC substrate do not collapse and Ni nanoparticles maintain their original morphology. Meanwhile, the unaggregated atomic Ni-N_4 sites remain in a highly dispersed state, verifying the microstructure is not destroyed under the long-time photocatalytic reaction.

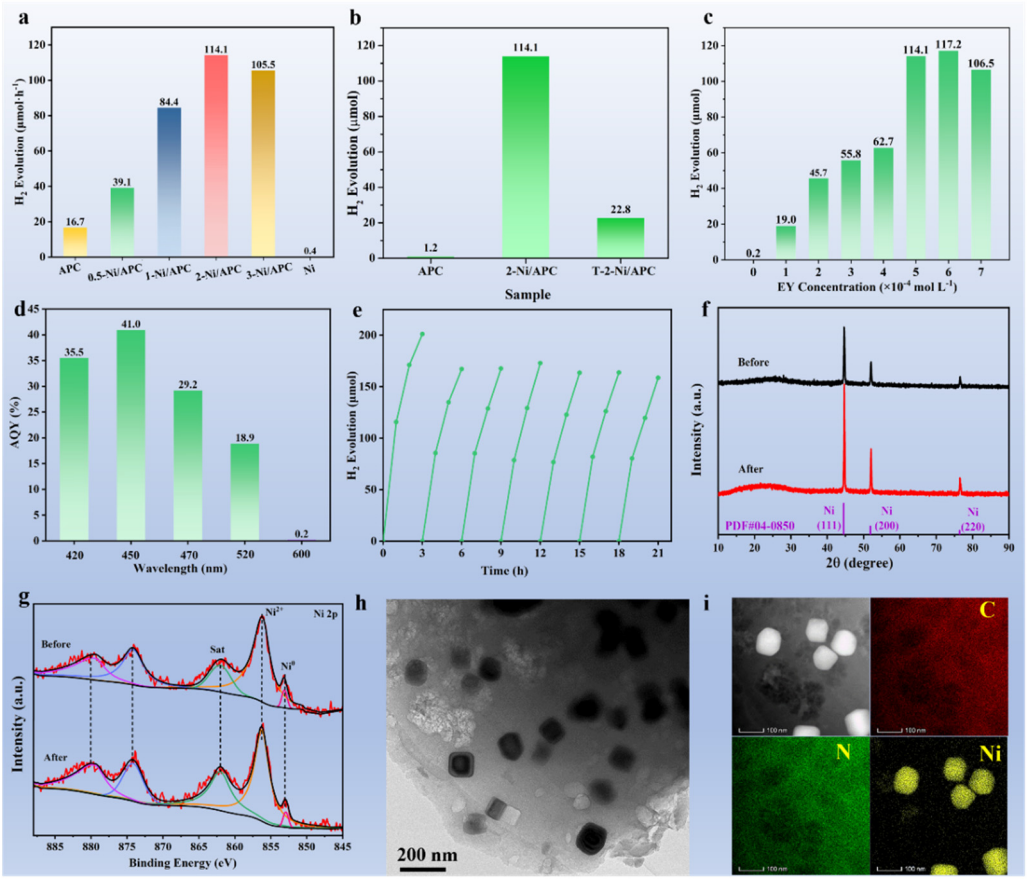

Figure 5. (a,b) Comparison of dye-sensitized photocatalytic hydrogen production activity for different samples; Effect of (c) dye concentration and (d) incident wavelengths on the hydrogen evolution activity; (e) Time courses of photocatalytic H_2 evolution for EY-sensitized 2-Ni/APC catalyst. (f) XRD patterns, and (g) Ni 2p XPS spectra of fresh and cycled 2-Ni/APC cocatalyst. (h) TEM image and (i) elemental maps of cycled 2-Ni/APC cocatalyst.

In order to observe the effect of different Ni amount on dye-sensitized HER activity, we also investigated the intrinsic electrocatalytic activity. Figure 6a gives the LSV curves of APC and x-Ni/APC catalysts in 1.0 M KOH solution. APC catalyst shows the worst electrocatalytic activity. After loading metal Ni, the x-Ni/APC catalysts show much enhanced electrocatalytic activities, confirming Ni components promote HER kinetics. The optimal 2-Ni/APC possesses the lowest overpotential of 280 mV at 10 mA cm^{-2}. In order to investigate the role of atomic Ni and metal Ni nanoparticles, LSV curves of T-2-Ni/APC and 2-Ni/APC are carried out. As presented in Figure S6, T-2-Ni/APC shows the higher electrocatalytic HER activity than APC, indicating that atomic Ni sites promote HER

 doi:10.20944/preprints202512.1450.v1

process. However, its activity is much lower than 2-Ni/APC, confirming that metal Ni nanoparticles play an important role of HER activity. The electrochemically active specific surface areas (ECSA) of these catalysts are compared by calculating the electrochemical double-layer capacitances (Cdl) values from CV tests in non-Faraday region. As seen in Figure 6b, 2-Ni/APC catalyst possesses the highest Cdl value, suggesting the highest ECSA (2.49 mF cm^{-2}), which is beneficial to dye adsorption, especially on atomic Ni-N sites with positive electrical property of Ni. Figure 6c shows the Nyquist plots of APC and Ni/APC composites. The semi-circle in high frequency region represents the charge transport resistance (RCT) between the electrode and electrolyte interface, which is used to measure the charge transport ability of the catalyst [39]. APC has the largest radius, suggesting the largest RCT. And the composites present the smaller semicircles, indicative of the decreased RCT. Atomic and nanoparticles Ni loaded on APC could effectively improve the electron transport. 2-Ni/APC composite has the smallest radius, which indicates the smallest RCT on the contact surface between 2-Ni/APC and the solution. The highest ECSA and lowest RCT are highly beneficial for the adsorption of dyes and the transmission of dye electrons. Figure 6d gives the adsorption amount of EY on different samples. APC has the smallest adsorption amount for EY, just 0.12 μmol g^{-1}, while Ni/APC cocatalysts present much higher EY adsorption amounts. The adsorption capacity of 2-Ni/APC to EY reaches the maximum value of 3.96 μmol g^{-1}, about 33 folds that of APC. Ni-N_4 sites in Ni/APC possess the positive charged $Ni^{\delta+}$, which acts as the site for adsorbing EY molecule owing to their electrostatic interaction. The T-2-Ni/APC catalyst has the higher ability for adsorbing EY molecules compared with 2-Ni/APC, confirming Ni-N_4 species as the adsorbed sites. Figure 6e provides the fluorescence spectra of EY solution before and after addition of the x-Ni/APC composites to confirm the electron transfer ability. Pure EY solution displays the high fluorescence emission intensity at 542.0 nm, suggesting the strong recombination of the photoinduced electrons and holes. After addition of APC, the intensity decreases, indicative of the photo-generated electrons transfer to APC. Furthermore, with the presence of x-Ni/APC composites in EY solution, the fluorescence intensity further decreases. The intensity in the EY/2-Ni/APC system shows the largest attenuation, which indicates its strongest electron transfer ability. Moreover, the blueshift of the emission peak also affirms their interaction [40]. Photocurrent intensity of APC and Ni/APC cocatalysts sensitized by EY were also observed. As shown in Figure 6f, Ni/APC cocatalysts show higher dye-sensitized photocurrent densities compared with APC. These results prove that metal Ni loaded (atomic and particled Ni) on APC can effectively promote the electron transport. The lowest overpotential, highest C_{dl} vaule, lowest RCT and the most efficient dye-produced electrons transport of 2-Ni/APC endow with its best dye-sensitized photocatalytic HER activity.

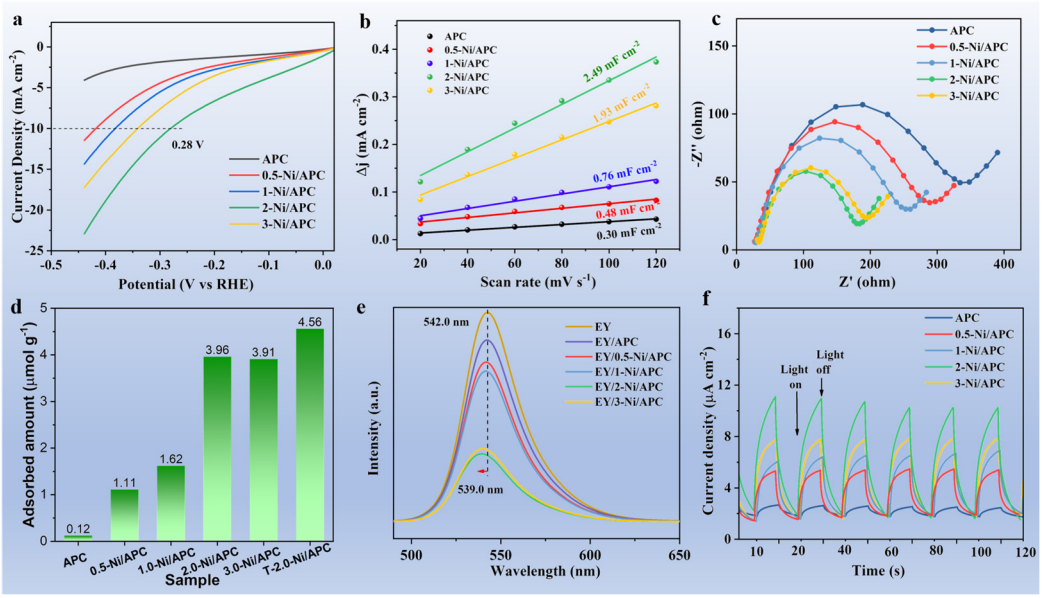

 doi:10.20944/preprints202512.1450.v1

Figure 6. (a) LSV curves, (b) the calculated Cdl values, and (c) Nyquist plots of different catalysts in 1.0 M KOH solution. (d) Dye adsorbed amount on different catalysts. (e) PL spectra of EY before and after addition of cocatalysts. (f) Photocurrent density of dye-sensitized APC and Ni/APC cocatalysts.

Thus, we propose the possible mechanism of the dye-sensitization HER, as illustrated in Figure 7. The adsorbed EY molecules on the Ni-N_4 sites via electrostatic interaction are irradiated to produce the excited EY state (EY*). Then, EY* could directly transfer their electrons to Ni-N4 species, and itself transforms to EY^+ which could be return to the ground sate with the presence of TMA donor. Owing to $Ni^{\delta+}$ in Ni-N_4, H_2O molecules are preferentially adsorbed on atomic Ni-N_4 sites, and dissociated into H^+ and OH^- [41,42]. The protons accept the electrons to form hydrogen atoms (H_{ads}), however, the strong binding energy of H atom on atomic Ni-N_4 is not conducive to equilibrium of adsorption and desorption for hydrogen atoms [43]. Figure S7 shows the T-2-Ni/APC exhibits the low electrocatalytic HER activity in 0.5 M H_2SO_4, proving that single Ni-N_4 sites are detrimental to hydrogen evolution. Thus, these Hads atoms diffuse to nearby Ni nanoparticles owing to its lower binding energy [44]. Finally, they bind together into H_2 and release from metal Ni sites. The components of single atomic Ni-N_4 and Ni nanoparticles serve as the different active sites, synergistically improving the activity for hydrogen evolution.

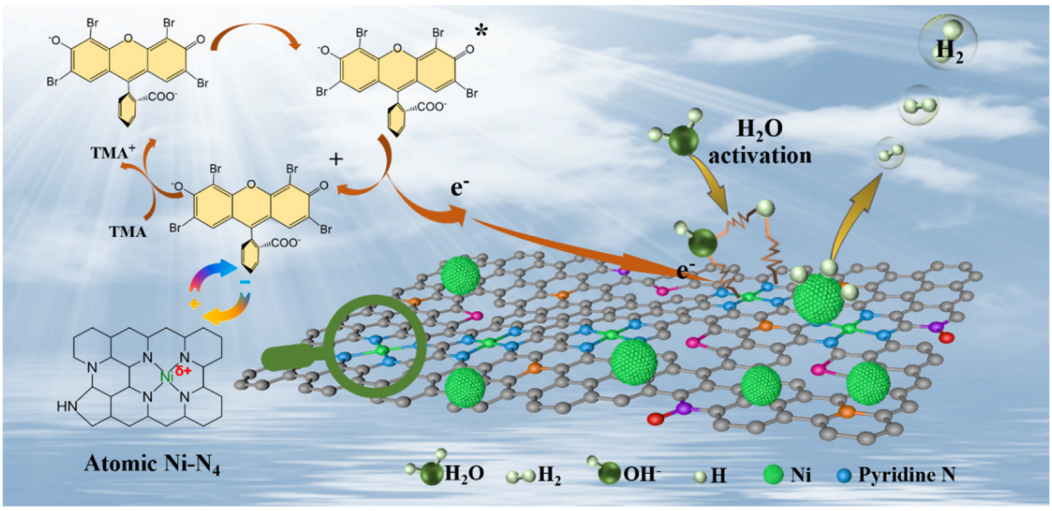

Figure 7. Possible mechanism of dye-sensitized photocatalytic hydrogen evolution for Ni/APC cocatalyst.

4. Conclusions

In this study, we have fabricated N-doped biomass carbon-based catalysts with metal Ni nanoparticles and atomic Ni-N4 sites derived from agaric/NiCl2 precursor via a facile hydrothermal-carbonization approach. The added NiCl2 as a self-template improves the formation of pores which is beneficial to the mass transfer diffusion. Importantly, the single atomic Ni-N4 species (strong metal-support interaction) are in situ formed and highly dispersed on biomass carbon sheets, and serve as the active sites for adsorbing EY molecules and reactant H2O, leading to effective electron transfer and promoting the water dissociation. And metal Ni nanoparticles undertake the active sites for H2 desorption. As a result, the obtained Ni/APC cocatalysts exhibit the much more efficient dye-sensitized photocatalytic HER activities, compared with pure APC, pure Ni, and atomic Ni/APC, fully demonstrating the synergistic effect of Ni nanoparticles and atomic Ni species. The optimal 2-Ni/APC cocatalyst shows a high AQY of 41.0 % with an excellent long-term stability for performance and structure, attributed to its lowest overpotential, highest ECSA, lowest charge transport resistance, and the most efficient dye-produced electrons transport. Our work provides insights into the design of efficient noble-metal-free HER catalysts by taking advantages of abundant biomaterials.

 doi:10.20944/preprints202512.1450.v1

Supplementary Materials: The following supporting information can be downloaded at the website of this paper posted on Preprints.org. Figure S1: SEM images for (a) 1-Ni/APC, (b) 2-Ni/APC, and (c) 3-Ni/APC composites; Figure S2: Adsorption-desorption isotherms of (a) APC and (b) 2-Ni/AP; Figure S3: XRD pattern of T-2-Ni/APC; Figure S4: (a) XPS survey of 2-Ni/APC, (b) C 1s and (c) N 1s spectra for APC and 2-Ni/APC, (d) Ni 2p spectra for Ni and 2-Ni/APC; Figure S5: The diagram of Ni-N_4 structure; Figure S6: (a) C 1s and (b) N 1s spectra for fresh and cycled 2-Ni/APC composite; Figure S7: LSV curves of APC, 2-Ni/APC, and T-2-Ni/APC in 1.0 M KOH solution; Figure S8: LSV curve of T-2-Ni/APC in 0.5 M H2SO4 solution; Table S1: Comparison of dye-sensitization photocatalytic hydrogen production activities for different carbon-based catalysts.

Author Contributions: Conceptualization, W.Y.Z. and Y.X.L.; methodology, T.L. and N.N.G.; validation, W.Y.Z. and S.Q.P.; formal analysis, T.L. and N.N.G; investigation, N.N.G. and S.Y.L.; data curation, S.Q.P. and Y.X.L.; writing—original draft preparation, W.Y.Z.; writing—review and editing, Y.X.L.; visualization, W.Y.Z.; supervision, Y.X.L.; funding acquisition, W.Y.Z. and Y.X.L. All authors have read and agreed to the published version of the manuscript.

Funding: Please add: This research was funded by National Natural Science Foundation of China (22369012, 21962010), Natural Science Foundation of Jiangxi Province (20242BAB25163) and the Key Laboratory Foundation of Jiangxi Province for Environment and Energy Catalysis (20242BCC32041).

Data Availability Statement: The original contributions presented in this study are included in the article and Supplementary Material. Further inquiries can be directed to the corresponding authors.

Conflicts of Interest: The authors declare no conflicts of interest.

References

1. Zhang, W.Y.; Ai, P.; Yuan, L.W.; Peng, S.Q.; Li, Y.X. In-situ converting CoO@Co/RGO into Co/$Co(OH)_2$/RGO for improved dye-sensitized photocatalytic H_2 evolution. *Fuel* **2024**, *369*, 31785.
2. Zeng, D.D.; Li, Y.X. Precisely loading Pt on Tb_4O_7/CN heterojunction for efficient photocatalytic overall water splitting: design and mechanism. *Appl. Catal. B-Environ.* **2024**, *342*, 123393.
3. Li, S.Q.; Peng, S.Q.; Li, Y.X. Constructing an open-structured J-type $ZnIn_2S_4$/$In(OH)_3$ heterojunction for photocatalytical hydrogen generation. *J. Phys. Chem. Lett.* **2024**, *15*, 5215-5222.
4. Zhang, W.Y.; Peng, S.Q.; Li, Y.X. Template-free synthesis of hollow Ni/reduced graphene oxide composite for efficient H_2 evolution. *J. Mater. Chem. A* **2017**, *5*, 13072-13078.
5. Jia, M.Z.; Lu, G.X. 750 nm visible light-driven overall water splitting to H_2 and O_2 over boron-doped Zn_3As_2 photocatalyst. *Appl. Catal. B-Environ.* **2023**, *338*, 123045.
6. Lazaar, N.; Wu, S.M.; Qin, S.S.; Hamrouni, A.; Sarma, B.B.; Doronkin, D.E.; Denisov, N.; Lachheb, H.; Schmuki, P. Single-atom catalysts on C_3N_4: minimizing single atom Pt loading for maximized photocatalytic hydrogen production efficiency. *Angew. Chem. Int. Ed.* **2025**, *64*, e202416453.
7. Fang, Y.X.; Wang, X.C. Peroxide production by porphyrins. *Nat. Energy* **2023**, *8*, 325-326.
8. Shi, H.R.; Yan, B.; Xu, H.K.; Li, H.; He, Y.; Liu, D.; Yang, G. $NiCS_3$: a cocatalyst surpassing Pt for photocatalytic hydrogen production. *J. Colloid Interf. Sci.* **2024**, *659*, 878-885.
9. Zhang, W.Y.; Mei, X.; Yuan, L.W.; Wang, G.; Li, Y.X.; Peng, S.Q. Tuning metal-support interaction of NiCu/graphene cocatalysts for enhanced dye-sensitized photocatalytic H_2 evolution. *Appl. Surf. Sci.* **2022**, *593*, 153459.
10. Xu, B.B.; Fu, X.B.; You, X.M.; Zhao, E.; Li, F.F.; Chen, Z.; Li, Y.X.; Wang, X.L.; Yao, Y.F. Synergistic promotion of single-atom Co surrounding a PtCo alloy based on a g-C_3N_4 nanosheet for overall water splitting. *ACS Catal.* **2022**, *12*, 6958-6967.
11. Li, Y.X.; Yang, T.Y.; Li, H.; Tong, R.; Peng, S.Q.; Han, X. Transformation of Fe-B@Fe into Fe-B@Ni for efficient photocatalytic hydrogen evolution. *J. Colloid Interf. Sci.* **2020**, *578*, 273-280.
12. Sun, Y.J.; Liu, X.T.; Zhao, X.J.; Wang, X.J.; Zhao, J.; Li, Y.P.; Mu, H.Y.; Li, F.T. The tuned Schottky barrier of a CoP co-catalyst via the bridge of ohmic contact from molybdenum metal for enhanced photocatalytic hydrogen evolution. *J. Mater. Chem. A* **2024**, *12*, 28830-28842.

 doi:10.20944/preprints202512.1450.v1

13. Lv, X.D.; Li, X.T.; Yang, C.; Ding, X.; Zhang, Y.; Zheng, Y.Z.; Li, S.; Sun, X.; Tao, X. Large-size, porous, ultrathin NiCoP nanosheets for efficient electro/photocatalytic water splitting. *Adv. Funct. Mater.* **2020**, *30*, 1910830.
14. Zhang, W.Y.; Li, W.T.; Li, Y.X.; Peng, S.Q.; Xu, Z. One-step synthesis of nickel oxide/nickel carbide/graphene composite for efficient dye-sensitized photocatalytic H_2 evolution. *Catal. Today* **2019**, *335*, 326-332.
15. Blach, D.D.; Kern, D.B.S.; Wang, B.P.; Long, R.; Ma, Q.; Prezhdo, O.V.; Blackburn, J.L.; Huang, L. Long-range charge transport facilitated by electron delocalization in MoS_2 and carbon nanotube heterostructures. *ACS Nano* **2025**, *19*, 3439-3447.
16. Fu, H.; Tian, J.; Zhang, Q.Q.; Zheng, Z.; Cheng, H.; Liu, Y.Y.; Huang, B.B.; Wang, P. Single-atom modified graphene cocatalyst for enhanced photocatalytic CO_2 reduction on halide perovskite. *Chin. J. Catal*. **2024**, *64*, 143-151.
17. Wu, Z.K.; Wang, T.Z.; Zou, J.J.; Li, Y.D.; Zhang, C.J. Amorphous nickel oxides supported on carbon nanosheets as high-performance catalysts for electrochemical synthesis of hydrogen peroxide. *ACS Catal.* **2022**, *12*, 5911-5920.
18. Kang, Q.L.; Li, M.Y.; Wang, Z.R.; Lu, Q.Y.; Gao, F. Agaric-derived N-doped carbon nanorod arrays@nanosheet networks coupled with molybdenum carbide nanoparticles as highly efficient pH-universal hydrogen evolution electrocatalysts. *Nanoscale* **2020**, *12*, 5159-5169.
19. Xu, Y.; Zhang, H.Y.; Zhang, P.; Liu, M.; Xie, X.J.; Huang, L. In situ exsolved Co components on wood ear-derived porous carbon for catalyzing oxygen reduction over a wide pH range. *J. Mater. Chem. A* **2021**, *9*, 10695-10703.
20. Yi, J.L.; Song, F.X.; Zhou, L.J.; Chen, Q.L.; Pan, L.; Yang, M. $Co_{1-x}S/Co_3S_4$@N, S-co-doped agaric-derived porous carbon composites for high-performance supercapacitors. *Electrochim. Acta* **2022**, *426*, 140825.
21. Zhang, H.; Zhang, Z.; Qi, X.T.; Yu, J.; Cai, J.X.; Yang, Z.Y. Manganese monoxide/biomass-inherited porous carbon nanostructure composite based on the high water-absorbent agaric for asymmetric supercapacitor. *ACS Sustainable Chem. Eng*. **2019**, *7*, 4284-4294.
22. Qi, X.T.; Zhang, H.; Li, C.; Chen, D.L.; Sun, C.H.; Yang, Z.Y. A simple and recyclable molten-salt route to prepare superthin biocarbon sheets based on the high water-absorbent agaric for efficient lithium storage. *Carbon* **2020**, *157*, 286-294.
23. Yang, C.; Cui, Y.; Su, Y.; Cheng, Y.; Yao, D.; Liao, Y.; Liu, S.; Fang, Y.; Wu, Y.; Wang, X.; Song, Y.; Lu, G.; Li, Z. Constructing a strong interfacial interaction in a Rh/RGO catalyst to boost photocatalytic hydrogen evolution under visible light irradiation. *ACS Appl. Energy Mater.* **2023**, *6 (11)*, 6317-6326.
24. Jannath, K.A.; Shim, K.; Seo, K.D.; Saputra, H.A.; Lee, S.M.; Kim, H.J.; Park, D.S. A multifunctional Mo-N/Fe-N interfaced MoS_2/FeNC electrocatalyst for energy conversion applications. *J. Mater. Chem. A* **2025**, *13*, 10899-10909.
25. Zhai, X.Y.; Wang, K.N.; Yuan, C.; Chen, P.F.; Zhao, W.; Wang, A.J.; Zhao, L.; Zhu, W.H. Innovative bipyridine-bridged metal porphyrin polymer for robust and superior electrocatalytic hydrogen evolution. *Chem. Commun*. **2025**, *61*, 5998-6001.
26. Zhou, T.; Han, X.; Shen, W.W.; Ji, F.; Liu, M.L.; Song, Y.Y.; He, W.W. Construction of NiS/CTF heterojunction photocatalyst with an outstanding photocatalytic hydrogen evolution performance. *Chin. Chem. Lett*. **2024**, *9*, 110415.
27. Kim, D.W.; Kil, H.S.; Kim, J.; Mochida, I.; Nakabayashi, K.; Rhee, C.K.; Miyawaki, J.; Yoon, S.H. Highly graphitized carbon from non-graphitizable raw material and its formation mechanism based on domain theory. *Carbon* **2017**, *121*, 301-308.
28. Zhao, P.; Yu, S.J.; Zhang, Y.S.; Cheng, H.; Yang, X.X.; Li, Q.H.; Zhang, Y.G.; Zhou, H. Ni transformation and hydrochar properties during hydrothermal carbonization of cellulose. *Fuel* **2025**, *382*, 133772.
29. Guo, J.; Hou, Y.J.; Li, B. Facile synthesis of a hollow Ni–Fe–B nanochain and its enhanced catalytic activity for hydrogen generation from $NaBH_4$ hydrolysis. *RSC Adv*. **2018**, *8*, 25873-25880.
30. Han, Q.; Leng, Y.M.; Zhai, L.L.; Bao, C.Z.; Zhang, J.L.; Hou, J.K.; Xiang, Z.H. Hierarchical pore engineering of MOF-5 derived electrocatalysts with high mass transfer for zinc-air flow batteries. *Int. J. Hydrogen Energy* **2024**, *71*, 165-173.

 doi:10.20944/preprints202512.1450.v1

31. Cai, Z.W.; Du, P.; Liang, W.H.; Zhang, H.; Wu, P.; Cai, C.X.; Yan, Z.J. Single-atom-sized Ni–N_4 sites anchored in three-dimensional hierarchical carbon nanostructures for the oxygen reduction reaction. *J. Mater. Chem. A* **2020**, *8*, 15012-15022.
32. Bulushev, D.A.; Nishchakova, A.D.; Trubina, S.V.; Stonkus, O.A.; Asanov, I.P.; Okotrub, A.V. Ni-N_4 sites in a single-atom Ni catalyst on N-doped carbon for hydrogen production from formic acid. *J. Catal*. **2021**, *402*, 264-274.
33. Meng, H.B.; Wu, B.; Zhang, D.T.; Zhu, X.H.; Luo, S.Z.; You, Y.; Chen, K.; Long, J.C.; Zhu, J.X.; Liu, L.P.; Xi, S.B.; Petit, T.; Wang, D.S.; Zhang, X.M.; Xu, Z.C.; Mai, L.Q. Optimizing electronic synergy of atomically dispersed dual-metal Ni-N4 and Fe-N4 sites with adjacent Fe nanoclusters for high-efficiency oxygen electrocatalysis. *Energy Environ. Sci*. **2024**, *17*, 704-716.
34. Feng, L.L.; Fu, C.L.; Li, D.M.; Ai, X.; Yin, H.Y.; Li, Y.H.; Li, X.Y.; Cao, L.Y.; Huang, J.F. High-density low-coordination Ni single atoms anchored on Ni-embedded nanoporous carbon nanotubes for boosted alkaline hydrogen evolution. *Dalton Trans.* **2023**, *52*, 9684.
35. Li, X.G.; Bi, W.T.; Chen, M.L.; Sun, Y.X.; Ju, H.X.; Yan, W.S.; Zhu, J.F.; Wu, X.J.; Chu, W.S.; Wu, C.Z.; Xie, Y. Exclusive Ni-N_4 sites realize near-unity CO selectivity for electrochemical CO_2 reduction. *J. Am. Chem. Soc.* **2017**, *139*, 14889-14892.
36. Feng, Y.C.; Long, S.S.; Chen, B.L.; Jia, W.L.; Xie, S.J.; Sun, Y.; Tang, X.; Yang, S.L.; Zeng, X.H.; Lin, L. Inducing electron dissipation of pyridinic N enabled by single Ni-N_4 sites for the reduction of aldehydes/ketones with ethanol. *ACS Catal*. **2021**, *11*, 6398-6405.
37. Yang, P.F.; Liu, F.S.; Zang, X.C.; Xin, L.T.; Xiao, W.P.; Xu, G.R.; Li, H.; Li, Z.J.; Ma, T.Y.; Wang, J.S.; Wu, Z.X.; Wang, L. Microwave quasi-solid state to construct strong metal-support interactions with interfacial electron-enriched Ru for anion exchange membrane electrolysis. *Adv. Energy Mater.* **2024**, *14*, 2303384.
38. Enoki, M.; Katoh, R. Estimation of quantum yields of weak fluorescence from eosin Y dimers formed in aqueous solutions. *Photochem. Photobiol. Sci*. **2018**, *17*, 793-799.
39. Yoo, Y.J.; Seo, D.H.; Baek, J.H.; Kang, M.J.; Kim, S.K.; Zheng, X.L.; Cho, I.S. Crystal reconstruction of Mo:$BiVO_4$: improved charge transport for efficient solar water splitting. *Adv. Funct. Mater*. **2022**, *32*, 2208196.
40. Zhang, W.Y.; Li, Y.X.; Peng, S.Q.; Cai, X. Enhancement of photocatalytic H_2 evolution of eosin Y-sensitized reduced graphene oxide through a simple photoreaction. *Beilstein J. Nanotech*. **2014**, *5*, 801-811.
41. Du, H.; Tian, D.X.; Zhao, J.J. Computational design of ternary NiO/MPt interface active sites for H_2O dissociation. *Int. J. Hydrogen Energy* **2022**, *47*, 20040-20048.
42. Li, P.; Zhao, G.Q.; Cui, P.X.; Cheng, N.Y.; Lao, M.M.; Xu, X.; Dou, S.X.; Sun, W.P. Nickel single atom-decorated carbon nanosheets as multifunctional electrocatalyst supports toward efficient alkaline hydrogen evolution. *Nano Energy* **2021**, *83*, 105850.
43. Liu, Z.C.; Cao, L.S.; Wang, M.L.; Zhao, Y.; Hou, M.; Shao, Z.G. A robust Ni single-atom catalyst for industrial current and exceptional selectivity in electrochemical CO_2 reduction to CO. *J. Mater. Chem. A* **2024**, *12*, 8331-8339.
44. Feng, L.L.; Fu, C.L.; Li, D.M.; Ai, X.; Yin, H.Y.; Li, Y.H.; Li, X.Y.; Cao, L.Y.; Huang, J.F. High-density low-coordination Ni single atoms anchored on Ni-embedded nanoporous carbon nanotubes for boosted alkaline hydrogen evolution. *Dalton Trans.* **2023**, *52*, 9684.